Allometric cell spreading and the geometrical control of focal adhesion collective organization

Célian Bimbard[1,†], Ali-Alhadi Wahhod[2,†], Démosthène Mitrossilis[3], Joseph Vermeil[1], Rémi Bousquet[4,5], Alain Richert[1], David Pereira[1], Pauline Durand-Smet[1], Sophie Asnacios[1], Jocelyn Étienne[2,✉], Atef Asnacios[1,✉], and Jonathan Fouchard[4,5,✉]

[1]Université Paris Cité, CNRS UMR 7057, Laboratoire Matière et Systèmes Complexes, Paris, France
[2]Université Grenoble Alpes, CNRS UMR 5588, Laboratoire Interdisciplinaire de Physique, Grenoble, France
[3]Biomedical Research Foundation of the Academy of Athens, Athens, Greece
[4]Sorbonne Université, CNRS UMR 8263, INSERM U1345, Development, Adaptation and Ageing, Paris, France
[5]Sorbonne Université, Institut de Biologie Paris Seine (IBPS), Paris, France
[†]These authors contributed equally to this work.

Focal adhesions are protein complexes that transmit actin cytoskeleton forces to the extracellular matrix and serve as signaling hubs that regulate cell physiology. While their growth is achieved through a local force-dependent process, the requirement of sustaining stress at the cell scale suggests a global regulation of the collective organization of focal adhesions. To investigate evidence of such large-scale regulation, we compared changes in cell shape and the organization of focal adhesion-like structures during the early spreading of fibroblasts either on a two-dimensional substrate or confined between two parallel plates, and for cells of different volumes. In this way, we reveal that the areal density of focal adhesions is conserved regardless of cell size or third-dimensional confinement, despite different absolute values of the surface covered by adhesion clusters. In particular, the width of the focal adhesions ring, which fills the flat lamella at the cell front, adapts to cell size and third-dimensional confinement and scales with cell-substrate contact radius. We find that this contact radius also adapts in the parallel-plate geometry so that the cumulated area of cell-substrate contact is conserved at the cell scale. We suggest that this behavior is the result of 3D cell shape changes which govern spreading transitions. Indeed, because of volume conservation constraints, the evolution of cell-body contact angle, adjusts according to cell size and confinement, whereas the rate of early spreading at the cell-substrate contact is not affected by third-dimensional geometry. Overall, our data suggest that a coordination between global and local scales mediates the adaptation of cell-substrate contacts and focal adhesions distribution to large scale geometrical constraints, which allows an invariant cell-substrate adhesive energy.

cell shape | focal adhesions | spreading | mechano-sensing | allometry

Correspondence: atef.asnacios@u-paris.fr jocelyn.etienne@univ-grenoble-alpes.fr jonathan.fouchard@sorbonne-universite.fr

Significance statement. Focal adhesions are micron-sized protein aggregates with which cells bind and communicate mechanical signals to their environment. Here, we reveal that the ratio between focal adhesions area and cell-substrate contact area is conserved independently of cell size or third-dimensional confinement, suggesting that cells maintain an invariant cell-substrate adhesive energy independently of internal or external geometrical constraints. Consistently, we find that the size of the lamella, a thin actin-rich sheet between the body of the cell and its leading edge, scales with the size of the cell-substrate contact. These allometric relationships demonstrate a major role of the global cell shape in the coordination of the growth of focal adhesions, allowing their adaptation during dynamic tissue rearrangement, like in regeneration or morphogenetic processes.

Introduction

In vivo, adherent cells encounter complex geometrical environments since the extra-cellular matrix (ECM) varies in density and topography in different organs (1, 2) and tissue physiological state (3, 4). The reconstitution of three-dimensional ECM networks *in vitro* has revealed that cell shape is influenced by the architecture of its micro-environment (4, 5). Because cell spreading modulates cellular functions such as traction force (6), differentiation (7) and cell cycle processes (8, 9), understanding the mechanisms which govern cell shape changes in complex geometrical environments is of particular importance.

Focal adhesions (FAs) represent a key player both for the definition of cell shape and cell mechano-sensing. FAs indeed form a mechanical connection between the acto-myosin cytoskeleton and the ECM, so that the clustering of FA components is necessary for the extension of cell-substrate contact area during spreading (10). On the other hand, FAs respond to the mechanical properties of the substrate through their force-dependent maturation involving the engagement of the integrin ligand, the recruitment of adaptor proteins (such as paxillin or vinculin) (11, 12) and the activation of associated signalling pathways (such as FAK phosphorylation) (8, 13). This process is realized locally in coordination with actin polymerization and myosin II accumulation at the cell leading edge (11, 14). However, the distribution of stresses that FAs collectively transmit to the substrate, as well as the force balance requested at the cell scale, suggest a global regulation of the organization of these structures (15, 16).

To understand this, we need to consider the biological players that govern cell shape changes at the cellular level. One of these players is the acto-myosin cortex, a thin cross-linked network which lies underneath the cell membrane of contact-free cell surfaces (17). A balance between cytosol pressure and an effective surface tension encompassing actin cortex

tension and cell adhesion, is then hypothesized to govern global cell shape through its curvature (18–20).

Only a few studies focused on the cooperation between the local clustering of adhesion proteins and three-dimensional cell-scale shape changes. In fully spread cells, it has been demonstrated that circumferential contractile actin arcs, originating from the cell front and linked to FAs, squeeze the cell body and acto-myosin cortex, pointing towards a local control of third-dimensional cell shape (21). On the other hand, in cells spreading between two micro-plates, we have shown that the macroscopic cell body contact angle is a good predictor of cell traction force and the subsequent formation of adhesion complexes (22). Along this line, a phenomenological rule has established a correlation between the distance from the cell edge to the center, traction stress and protrusion rate at the cell edge during cell polarization (23, 24).

Despite these findings, the question of how local and global-scale mechanical processes interplay to define cell shape at the cellular level remains largely unresolved. In this article, we study how three-dimensional cell shape, cell-substrate contact and collective organization of FAs are affected when large scale geometrical parameters of the cell or its environment are modified. We show that the cumulated areas of peripheral FA and cell-substrate contact are conserved whether cells spread confined between parallel plates or unconfined. By changing cell volume, we also demonstrate that these characteristic areas scale with cell size. These effects correlate with changes in cell-substrate contact angle in those conditions, variations which are determined by volume conservation. Finally, we found that allometric relationships between the extent of cell body spreading and lamella size are consistent with the conservation of FA density with respect to cell size and third-dimension confinement. These results demonstrate that the size of cell-substrate contact and collective organization of FAs are regulated by third-dimensional cell-scale geometrical constraints.

Results

Cumulated areas of FAs and cell-substrate contact are conserved in confined and unconfined spreading. We analyzed the early spreading of isolated Ref-52 fibroblasts in two different substrate configurations. In the first configuration, the cell is let free to spread on a bi-dimensional glass coverslip. The coverslip is coated with fibronectin to permit integrin engagement. In the second configuration, before the onset of spreading, a glass plate with the same coating is positioned parallel to the coverslip at a distance h, with h close to the diameter L_0 of the cell while in suspension ($h/L_0 = 0.92 \pm 0.02$, N=15 cells). Thus, cells spread confined in between two parallel plates (Fig. 1-A). Ref-52 fibroblasts expressed a fusion of YFP with paxillin, a marker of FAs. We could thus visualize via TIRF microscopy the evolution of cell-substrate contact (thanks to cytoplasmic paxillin) and the formation of FA-like clusters (intense paxillin aggregates) in the vicinity of the substrate (lower plate only) during spreading in both configurations (Fig. 1-B).

In a previous work, we have examined the series of events taking place during spreading in the single plate geometry (22). Briefly, we found that spreading occurs in two phases as previously described (25–27), with a first rapid phase (P1) where cell radius increases proportionally to time (Fig. S1). This phase is followed by a slower phase (P2) after about 450 s of spreading. The slow-down of cell spreading occurs moments after a transition in paxillin organization, with paxillin aggregates evolving from transient dot-like patches uniformly distributed into elongated aggregates, dense in paxillin and analog to FAs, situated at the cell front (Fig. 1-C, top, Supplementary movie 1).

These features are also observable when cells spread confined between parallel plates (Fig. 1-C and 1-D, Supplementary movie 2). First, a ring of paxillin clusters appears after minutes of spreading. Second, the spreading process displays two phases; importantly, the rate of spreading during P1 is unchanged by the addition of the upper plate ($v^{1p} = (3.0 \pm 0.2) \times 10^{-2} \mu m \cdot s^{-1}$, N=34; $v^{2p} = (2.7 \pm 0.2) \times 10^{-2} \mu m \cdot s^{-1}$, N=45, p-value = 0.33 for two-sided Mann-Whitney test, Fig 1-D and S1-B). However, in the parallel-plate geometry, the transition in spreading regime and peripheral FA ring formation occur at contact areas approximately twice smaller than in the single-plate geometry (factor 2.0 ± 0.2 for the mean contact area at FAs transition $A(t^*_{adh})$; factor 2.4 ± 0.3 for the mean contact area at spreading transition $A(t^*_R)$, Fig 1-C, 1-D and 1-E). In addition, when spreading has saturated for most cells in both conditions (i.e after 20 minutes), the cell-substrate contact area differs when in confinement, being reduced by a factor 2.2 ± 0.2 in the parallel-plate geometry (Fig 1-C, 1-D and 1-E, and see Fig S1-C for a population representation). It is worth noting that, building on the fact that cells spread similarly on both plates when in a parallel plate geometry (28), the total contact area with the plates is expected to be twice the area measured on the bottom plate here. This implies that the characteristic contact areas of spreading are conserved, irrespective of whether the spreading is in a confined or unconfined geometry.

We next tested whether this accommodation of cell contact area to third-dimensional confinement was accompanied by changes in the surface occupied by FA-like clusters. We found that after saturation of spreading (20 minutes), the contact area occupied by FAs (which we denote S_{pax}) also adapts to confinement: the total surface occupied by adhesion measured in confined geometry is reduced by a factor 1.8 ± 0.2 as compared to unconfined spreading (Fig 1-C, 1-F and 1-G), suggesting that the cumulated area of FAs on both plates in the confined spreading is equal to the one measured in unconfined (bi-dimensional) spreading. It is important to note that this adaptation of the area of the FA ring occurs while the local cellular environment (glass plates coated with fibronectin) is unchanged between confined and unconfined configurations.

Finally, since cell-generated traction forces are known to adapt to the stiffness of the substrate (28, 29), we investigated, in the parallel plate confined geometry, whether the stiffness of the flexible plate has an impact on the character-

istic cell-substrate contact areas (Fig. S2-A). It turns out that, although the maximum cell traction force and the maximum rate of force increase both increase significantly with stiffness (Fig. S2-B and S2-C), stiffness has little or no effect on the evolution of cell-substrate contact and distribution of FAs (Fig. S2-D to S2-H). Therefore, the measurements we present here include data obtained with three different stiffness values (1.5 nN/μm, 12.5 nN/μm and infinite stiffness - achieved through feedback-loop control (30)) but we restrict our analysis to the effect of substrate geometry.

Cell-substrate contact and total FA areas scale with cell size. The above results suggest that cell-scale geometrical constraints determine the overall size of cell-substrate contact and collective organization of FAs. To further test this hypothesis, we varied cell volume and analyzed the evolution of cell-substrate contact on bi-dimensional substrates (Fig. 2-A). Varying cell volume also has physiological relevance since volume varies along cell cycle (31, 32) and according to nutrient conditions (33). We induced the formation of larger cells by culturing them with a low dose of Mitomycin C (MMC), which blocks mitosis without inhibiting protein synthesis (34). On average, before spreading, MMC-treated cells have a 2-fold increase in their apparent surface $A_0 = 4\pi R_0^2$, with R_0 the cell radius in suspension, and a 2.8-fold increase in volume (Fig. S3-A to S3-C).

Spreading of MMC-treated cells exhibit the same qualitative characteristics as the one of non-treated cells (Fig. 2-B, 2-C, Fig. S3-D and Supplementary movie 3). Like in the confined geometry, the spreading rate during P1 is not significantly modified by changes in cell size ($v_{\text{Unt}}^{\text{1p}} = (3.0 \pm 0.2) \times 10^{-2} \mu\text{m} \cdot \text{s}^{-1}$, N=34; $v_{\text{MMC}}^{\text{1p}} = (3.8 \pm 0.4) \times 10^{-2} \mu\text{m} \cdot \text{s}^{-1}$, N=21, p-value = 0.11 for two-sided Mann-Whitney test, Fig. 2-C, Fig. S3-E). This is in agreement with the hypothesis that the extension of the lamellipodium is controlled locally by actin polymerization during this phase (22), and that this phase is characterized by non-specific interactions with the substrate (26). However, the areas characterizing spreading are increased in MMC-treated cells compared to untreated cells, by a factor 1.5 ± 0.2 for $A(t_{\text{adh}}^*)$, which characterizes the onset of FA maturation, and by a factor 2.3 ± 0.3 for $A(t_R^*)$, which characterizes the spreading slow-down (Fig. 2-C and 2-D). The dependence of these characteristic areas according to cell size was confirmed when analyzing cells individually with respect to their apparent surface in suspension A_0. We found that both $A(t_{\text{adh}}^*)$ and $A(t_R^*)$ scale with A_0 but with a different exponent: $A(t_{\text{adh}}^*) = 3.3 \ A_0^{0.76}$ and $A(t_R^*) = 0.06 \ A_0^{1.4}$ (Fig. 2-E and 2-F). Consequently, the difference in contact area between these two events also increase with cell size (Fig. 2-G). Note also that the exponent 1.4, close to 1.5, suggests that cell contact area at spreading transition scales like cell volume (Fig. S3-F).

Finally, at saturation of spreading, the cumulated area of the peripheral paxillin clusters S_{pax} increases following MMC treatment, in proportion with the increase of cell contact area A: factor 2.0 ± 0.2 for $S_{\text{pax}}(t=20\text{min})$ and 1.8 ± 0.2 for $A(t=20\text{min})$ (Fig. 2-D, 2-H and 2-I).

FA areal density is conserved irrespective of cell size and third-dimension confinement. The observation that, at the final stage of spreading, both cell substrate contact area and area of FA ring are rescaled in the same way in confined and unconfined geometry, and whether cells are treated with MMC or not, implies that the ratio $S_{\text{pax}}/A(t = 20\text{min})$ is a conserved quantity. In fact, in all these conditions, the area occupied by the peripheral ring of FAs represents about one tenth of the cell-substrate contact area: 0.09 ± 0.01 for single plate geometry, 0.12 ± 0.01 for parallel plates geometry and 0.10 ± 0.01 for MMC-treated cells (Fig. 2J).

Intra-population comparison over these different conditions confirm that such an adaptation occurs even at the single cell level (Fig. 3-A). A linear regression on the pooled data gives a prefactor equal to 0.09, very close to the mean values of $S_{\text{pax}}/A(t = 20\text{min})$ obtained for each condition. This conservation of the FA areal density is surprising since FAs are mainly distributed along cell perimeter and, therefore, we would rather expect the ratio of cumulated FA area over cell perimeter $S_{\text{pax}}/(2\pi R(t = 20\text{min}))$ to be conserved. Since this is not the case, a non-trivial process must govern the collective organization of FAs and its adaptation to cell-scale geometrical constraints.

We propose a model to comprehend how this cumulated FA area scales like the total contact area, regardless of cell and substrate geometry (Fig. 3-A). In line with other theoretical work (35, 36), we assume that, during early spreading, before the cell polarizes, FAs form at constant density d_{adh} along the contact line. Thus, when a new row of FAs forms, the number of FAs (N_{FA}) varies like :

$$dN_{\text{FA}} = 2\pi d_{\text{adh}} r dr \tag{1}$$

Integrating over the width of the FA ring (which we denote W_r), we have :

$$N_{\text{FA}} = 2\pi d_{\text{adh}} \int_{R-W_r}^{R} r \, \mathrm{d}r \tag{2}$$

We observed that the area of individual adhesion clusters s_{pax} is constant in the different substrate or cell geometries tested (Fig. 3-B). Consequently, the cumulated area of FAs is :

$$S_{\text{pax}} = s_{\text{pax}} N_{\text{FA}} = \pi d_{\text{adh}} s_{\text{pax}} (2RW_r - W_r^2) \tag{3}$$

For the ratio $S_{\text{pax}}/A(t = 20min)$ to be constant, we then expect the width of the FA ring W_r to be proportional to the cell contact radius R.

To test this, we determined the width of the FA ring W_r by averaging paxillin intensity over cell contour and representing it as a function of the distance to the cell edge at each time-point of the spreading process (see Methods). Figures 3-C, 3-D and 3-E represent the spatio-temporal distribution of paxillin normalized by the maximum intensity along cell radius at each time-point for typical samples in the single plate, parallel plates and MMC-treated conditions respectively. At early time-points, the intensity is homogeneous over the cell-substrate contact, while, during the second phase of spreading, it is higher near the leading edge compared to the cell

central region. To determine the position of the inner boundary of the paxilin ring, we used a threshold on the normalized intensity map corresponding to half the maximum intensity at each time-point of the second phase of spreading P2 (yellow lines, Fig. 3-C to 3-E). With this method, we found that the ratio of paxillin ring width over cell contact radius after 20 minutes of spreading $W_r/R(t = 20\text{min})$ was independent of substrate geometry or cell size (Fig. S4-A). This scaling was valid not only at 20 minutes but all along the second phase of spreading (Fig. 3-F). According to Equation (3), the scaling between paxillin ring width W_r and cell contact radius R could then explain the conservation of FA areal density, i.e how the surface of FAs S_{pax} scales like the contact area $A(t = 20\text{min})$.

In sum, our results point towards a cell-scale mechanism that regulates the size of the paxillin ring along with cell substrate contact radius, while both of these quantities adapt to cell size and third-dimensional confinement.

FA ring size depends on myosin II contractility, independently of spreading. Because FA growth is known to be mechanosensitive and myosin II-dependent, we next asked whether myosin contractility could regulate FA ring size. For that, we inhibited myosin II activity by incubating cells in the Rho-kinase inhibitor Y27632 before imaging spreading in TIRF (Fig. 4-A and Supplementary Movie 4). It is known that myosin II does not affect the first phase of spreading (22, 37). Here, lower cell contractility was associated with a less regular contour of the cell projected area, as shown in (37), however its size after 20 minutes of spreading was not different in Y27632-treated cells from the one of untreated cells ($A_{t=20min}^{Unt} = (1.77 \pm 0.07) \times 10^3 \mu\text{m}^2$, N=34; $A_{t=20min}^{Y27} = (1.79 \pm 0.09) \times 10^3 \mu\text{m}^2$, N=17, p-value = 1.00 for two-sided Mann-Whitney test, Fig. 4-B). Unsurprisingly, given the known role of myosin-generated force on focal adhesion maturation, the surface of paxillin ring S_{pax} was smaller in conditions of lower cell contractility, with a slight tendency to increase in cells of larger contact areas (Fig. 4-C). This could be due to the smaller, less elongated paxillin aggregates observed (Fig S4-B and S4-C) but also possibly to a less extended FA ring. Therefore, we measured the width of the paxillin ring over the second phase of spreading with the method previously described, based on fluorescence intensity (Fig. 4-D). We found that the ring was indeed thinner in conditions of lower contractility (Fig. 4-E), while the ratio of paxillin ring width over cell contact radius was significantly smaller than in untreated conditions, contributing to the smaller density of FAs (Fig. S4-A). Moreover, qualitative analysis of FA turnover suggests that FAs turnover faster when cell contractility is inhibited (Fig S4-B and S4-C). This effect could be at the origin of the reduced ring size observed. Altogether, this demonstrates that FA areal density is dependent on myosin II activity and that the ratio of FA ring size over cell-substrate contact radius is regulated by cell contractility.

The time-evolving 3D body shape of spreading cell scales with cell size and is affected by confinement.

Previous work revealed that cell body contact angle, a cell-scale parameter, dictates the onset of traction force generation and growth of FAs during spreading between parallel plates (22). Cell-substrate contact angle indeed reflects the equilibrium of tensions between the cell, its substrate and the medium. Therefore, we quantified the effect of cell confinement and cell size on the cell contact angle from profile views of the spreading process imaged in bright-field (Fig. 5-A and 5-B; Supplementary movies 5 & 6).

The automatized segmentation of cell profile and determination of contact angle is described in Methods (Fig. 5-C and Supplementary movie 7). Note that the contact radius measured here — which we name cell body contact radius and denote R_b on the figures because it corresponds to the apparent contact point between the cell body and the plates — does not correspond to the contact radius R measured by TIRF microscopy. Indeed, the extremity of the flat lamella at the cell front could not be detected in the profile view experiments realised in bright-field imaging (see Fig. 5-C).

As expected, the cell contact angle (see definition in Fig. 5-C) increased during spreading on a single plate. But, at equivalent contact radii, the cell contact angle was lower in MMC-treated cells compared to non-treated cells throughout spreading (Fig. 5-D). This is the case even for small contact radii corresponding to the first phase of spreading P1, during which the contact radius increases at the same rate in the two conditions (Fig. 2-C). Therefore, there is a discrepancy between the rate at which the contact with the plates and the cell contact angle increase in untreated and MMC-treated cells during the first phase of spreading. Nevertheless, after rescaling the contact radius by the radius of the cell in suspension R_0, the data of contact angle as function of the normalized contact radius collapse on a unique "master" curve (Fig. 5-E). This indicates that cell spreading follows the same dynamics, regardless of cell size or MMC treatment. Notably, those results also indicate that cell volume and cell contact angle cannot be regulated independently.

We next analysed how cell contact angle evolves in the context of cell confinement. Here, the contact angle as a function of contact radius increases with a larger slope when cells are confined between parallel plates than when they are free to spread on a single plate (Fig. 5-F). Like for MMC-treated cells, this effect is observable also during the early phase P1, although the cell-substrate contact areas increased at the same rate in both geometries during this phase of spreading (Fig. 1-D and Fig. S1-B). Thus, contact angle evolution is not only driven by cell-substrate contact interactions, but is also dictated by third-dimension confinement and cell size. Also, it appears that spreading transitions occur at lower contact areas when the contact angle evolves more rapidly. This is consistent with our previous findings showing that the growth of peripheral FAs closely follows the out-of-plane cell traction force, past a specific contact angle (close to 90°) (22).

Substrate geometry, volume conservation and isotropic cortical tension predict three-dimensional cell shape changes during spreading. To understand how cell size and substrate geometry could be at the origin

of these differences in three-dimensional cell shape changes, we designed a geometrical model of cell spreading (see details in Appendix 1 of Supplementary Materials and Fig. S5-A and S5-B). The modeling idea stems from the fact that cell body shape is known to result from the cortical tension (21), leading to a mechanical balance governed by Laplace law. Considering the radial symmetry of cell shape during early spreading, we then use the Young-Laplace equation :

$$H(t) = \frac{r''}{(1+r'^2)^{3/2}} - \frac{1}{r\sqrt{1+r'^2}} = \frac{\Delta p}{\sigma} \qquad \textbf{(4)}$$

where $r' = dr/dz$, Δp is the pressure difference between the interior and exterior and we define H the mean curvature. Making a further assumption of isotropic cortical tension (21, 38?) yields that H is uniform in space and the shape should be of constant mean curvature (CMC). For a given cell volume and for any cell body-substrate contact radius $R_b(t)$, there is a unique CMC shape, that is, a spherical cap in the unconfined geometry and a portion of either a nodoid or an unduloid in the confined geometry (Fig. S5-C). Assuming that the volume of the cell is conserved throughout spreading, equal to the values shown in Fig. S3-C for untreated and MMC cells respectively, we could thus make predictions of its shape evolution as a function of the cell body contact radius, either in unconfined or confined geometry (Fig. 6, Supplementary movies 8, 9 and 10). In particular, in this model, the data of volume and current cell contact radius are predictive of the contact angle independently of the cortical tension. This is because cell body pressure is expected to adjust in proportion to cortical tension, .

In the unconfined geometry, the dorsal arc radius evolves with cell contact radius consistently in the model and in measurements from live cells, indicating that the model can describe global cell shape changes in this configuration (Fig. S5-D). The size-independent evolution of the cell contact angle observed in untreated and MMC-treated cells were also well recapitulated by the geometrical model (Fig. 5-E, solid line). In addition, in the model of parallel plate spreading, the contact angle evolves faster as a function of cell contact radius than in the single plate geometry. Furthermore, the geometrical model reproduces the different rates of contact angle evolution observed in cells spreading on a single plate or in between parallel plates (Fig. 5-F, solid lines). Altogether, this shows that the different rates of three-dimensional cell shape changes, represented by the evolution of cell contact angle, can be explained by two geometrical ingredients acting at the local and global scales respectively: cell-substrate contact expansion, on the one hand, and volume conservation, on the other hand.

The cause leading to a size-dependent relation between cell body contact radius and contact angle is apparent when one considers that the shapes are self-similar when scaling the cell with its size, and that this self-similarity conserves angles whereas distances need to be rescaled. It is less obvious in general to determine how the presence of two plates rather than one only affects the contact angle. However, considering the stage of spreading for which the cell body makes a 90° angle with the substrate, the corresponding shapes of constant mean curvature are respectively a hemisphere and a cylinder of the same volume. In this case, a cylinder will have smaller a basal area, which accounts for the fact that contact angle increases faster in the parallel-plate configuration. Consequently, because of volume conservation, increasing cell confinement is akin to reducing cell size as far as the evolution of the three-dimensional cell shape is concerned. This could explain how those different geometrical perturbations affect the characteristic spreading areas in a similar way.

The lamella size scales with the cell body contact radius during spreading and coincides with FA ring. On the one hand, we show that the three-dimensional cell shape (quantified via the cell contact angle) adapts to cell size and third-dimensional confinement because of volume constraints; on the other hand, we observed that the width of the FA ring adapts to cell contact radius, regardless of geometrical confinement, and that this permits the conservation of FA areal density. We next wanted to identify a potential link between those cell-scale geometrical relationships in and out of the plane of spreading. Since FAs are found within a flat compartment, called the lamella, present at the leading edge of spreading cells (39) and because the distinction between cell body and lamella is based on their geometrical shape, we went on to quantify the sizes of these respective compartments along spreading. For that, we fixed cells at different time-points during spreading. An F-actin-rich flat compartment was indeed present at the cell leading edge at all stages of spreading (Fig. 7-A). The cell contact radius R was thus found to be composed of the cell body contact zone, of radius R_b, and the lamella of width W_l.

We first verified that cell fixation did not influence three-dimensional cell shape by measuring cell contact angle with respect to cell body radius R_b in fixed cells and live cells (Fig. S6-A and S6-B). Second, we found that the size W_l of the lamella increased along spreading, in proportion with the contact radius R_b and regardless of the phase of spreading (Fig. 7-B). Notably, the respective sizes of these two cell compartments (cell body and lamella) followed the same trend in MMC-treated cells, showing that this behavior was independent of cell size and contact angle progression.

Pooling the datapoints from untreated and MMC-treated cells together, a linear regression $W_l(t) = \beta R_c(t) + W_l^0$ indicated that $\beta = 0.45$ and $W_l^0 = 0.02$ μm (coefficient of determination $R^2 = 0.49$). This suggests that the sizes of the lamella and the contact region of the cell body are intrinsically linked. We could then compare the lamella size W_l to the width of the FA ring W_r. Note that, whereas the lamella is present and thus W_l is measurable at all stages of spreading, the width W_r is defined only when FAs have matured, thus during the second phase of spreading. Considering that $R = R_b + W_l$, we find that $\frac{W_l}{R} = \beta/(1+\beta) = 0.31$, very close to the ratio $\frac{W_r}{R}$ measured during the second phase of spreading (Fig. 3-F), which was equal to 0.37 ± 0.02 for the single plate geometry, 0.37 ± 0.03 for the parallel plate geometry and

0.35 ± 0.02 for the MMC-treated spreading on a single plate. Fig. 3-C to 3-E show the coincidence between the typical lamella size W_l (white dotted lines) and W_r (solid yellow lines). We conclude that, since $W_l(t) \simeq W_r(t)$ irrespective of cell size, FAs are located within the lamella during the slow spreading phase P2.

In summary, our data suggest that the growth of FAs is controlled by the cell contact angle, whose evolution depends on cell and substrate three-dimensional geometry. Because the cell-substrate contact area grows at the same rate during P1 independently of these constraints, then FAs start forming at different contact areas. Subsequently, while spreading proceeds, FAs mature and fill the lamella, whose size is proportional to the contact radius (see overlay of cell body reconstruction and lamella size on Fig. 7-C).

Discussion

Because fibroblasts evolve in complex and dynamic three-dimensional environments within tissues while being also subjected to changes of their own size along the cell cycle, they need to coordinate shape changes occurring at the cell scale (including cell body shape) together with changes in the size of the cell-substrate contact and the distribution of its adhesive structures. While cell shape changes are governed by molecular-scale actors (plasma membrane, cytoskeleton, adhesion complexes), it is still unclear whether these changes result simply from the integration of local-scale events at the cell scale or whether large-scale constraints could feed back on the local scale to control the dynamics of molecular actors. A major finding of this study is that the transition in FA organization and spreading rate (onset of paxillin clustering and spreading slow-down, respectively) scale like cell size, although with different exponents. In particular, the area characterizing spreading transition scales like cell volume (Fig. 2F). In addition, when cell spread between parallel plates, those characteristic transition areas are significantly modified on each plate individually but the cumulated surfaces over the two plates are unchanged compared to spreading over a single surface (Fig. 1E). This demonstrates that spreading slow-down and onset of FA assembly are not purely kinetic processes as previously suggested (40). Various hypotheses have been proposed so far that could potentially explain how a cell scale parameter could control the formation of FAs at the local scale.

First, theoretical work suggested that an increase in the length of the contact line could trigger FA clustering via a phase transition process relying on short-range protein bridging (36). In our system, FAs should then form at a conserved size of individual cell-substrate contacts irrespective of the substrate geometry (single plate or two parallel plates). However, our data show that FA assembly is rather triggered when the total cell-substrate area reaches a threshold that scales like cell size. Another mechanism of transition was proposed that would rely on a burst of plasma membrane tension after exhaustion of a pool of free membrane. That event could trigger the transition between the two phases of spreading, and subsequent growth of FAs (41). This is consistent with a spread-

ing transition occurring at a conserved total cell-substrate contact area, as observed here. However, although a sudden membrane flattening accompanies the transition from fast to slow cell spreading, these two events occur after the onset of FA formation (22). This sequence of events is confirmed by our data and even more compelling in the case of larger cells (Fig. 2G). Conversely, in some rare events (n/N=3/30) where spontaneous disassembly of a first ring of FAs happened after entering phase P2, it was correlated with an acceleration of cell spreading at a rate similar to P1, before FAs re-formed into a second, larger peripheral ring (Fig. S7 & Supplementary movie 11). These observations thus rather suggest that FA growth could be the cause rather than consequence of the spreading transition. Finally, a third mechanism that could trigger the formation of FAs is a change in the force balance at the cell scale, whereby the (possibly unchanged) actomyosin cortical tension which is internally balanced at the beginning of cell spreading starts being transferred to the substrate at some stage. In (22), we show that indeed FA formation coincides with the stage where the cell—substrate apparent contact angle reaches 90°, an angle beyond which internal balance of cortical tension becomes geometrically impossible.

Although the trigger of FA growth and maturation appears a global-scale mechanism, their individual growth has all the features of a local phenomenon. In agreement with previous findings showing that local traction forces generated by myosin II at the junction between the lamellipodium and the lamella control FA size (11, 14), we find that individual FAs have the same area when substrate geometry or cell size is changed. Consistently with (35, 36), their density along contact line also appears to be constant. Finally, there is no apparent variability in the intensity of each FA, suggesting that they carry the same adhesion energy. Taken together, these three local and invariant intensive characteristics (density, individual size and intensity) could lead to an invariant adhesive surface – and presumably adhesive energy – per unit area of the ring over which they are distributed. However, we find that, on the other hand, the total adhesive surface (cumulated FA area) scales with the total area of contact with the substrate, with a scaling parameter which is robust to the geometrical changes induced by confinement and cell size. Notably, the same effect has been observed on human foreskin fibroblasts confined on bi-dimensional adhesive islands of circular shapes (42). Here, the peripheral FA ring represented about 15% of the contact area, versus approximately 10% in our system. Maintaining such a scaling irrespective of whether the cell is confined or not requires a global regulation.

Thanks to 3D reconstruction of the geometry of the actin cortex, we determine the relative size of the lamella of cells at different stages of spreading. Surprisingly, we show that throughout the different phases of spreading, the lamella length scales with the spread radius of the cell body while they both undergo a more than 5-fold increase, thus being globally regulated whereas the leading edge protrusivity seems to be locally regulated. In order to coordinate the po-

sition of the body–lamella transition point, there is thus also the requirement for a global coordination mechanism able to conserve this observed allometry in coordination with leading edge progress. Future work could focus on the origin of this coordination, through an analysis of potential geometry-dependent cytoskeletal organizations, within the lamella and the cortex. The observation that FA ring width depends on myosin II contractility, suggests that the lamella size could adjust to internal tension as shown in crawling cells (21) possibly by modulating stability and turnover of FAs or a sub-population of them (Fig. S4-B and S4-C).

At all scales in biology, allometric relationships link the size of the parts or compartments of a system to the size of the entire system. For instance, such allometric relationships link the size of body segments to the size of organisms in insects (43) and tetrapods (44), but also the volume of organelles to the one of cells (45). Allometric scaling can then be used to identify the physical constraints underlying the mechanisms of growth. Regarding adhesion, total adhesive pad area is found to scale like organism mass over a wide variety of animal species, possibly to resist against body weight, a volumetric force (46). Here, at the cellular level, we demonstrate that the surface of the peripheral ring of adhesive sites scales like cell-substrate contact area, independently of cell size and substrate geometry (Fig. 3-A). Consistently, we find that the size of the lamella, a thin actin-rich sheet between the body of the cell and its leading edge, scales with the cell contact radius. These findings reveal a major role of the global cell shape in the coordination of the growth of focal adhesions. Unlike large multi-cellular organisms, cells are mainly subjected to surface forces generated internally by the tensile acto-myosin cytoskeleton or externally by neighboring cells. Although it is unknown how the scaling relationships we identify here transfers to the three-dimensional contexts that fibroblasts encounter in vivo, when extra-cellular matrix covers cell body continuously, the invariance of focal adhesion areal density could prevent cell delamination (47) and maintain tissue integrity during dynamic tissue rearrangements such as regeneration or wound healing.

Methods

Cell culture and mitomycin C treatment. Rat embryonic fibroblasts (Ref-52) stably expressing paxillin-YFP were grown using DMEM supplemented with 10% (vol/vol) heat-inactivated FCS, 2 mM glutamin, 50 units/mL penicillin, and 50 g/mL streptomycin. All cultures were maintained at 37°C under humidified 5% CO2 atmosphere. To increase cell volume, Mitomycin-C (Sigma, M4287) at a concentration of 0.25μM was introduced into culture medium for 2 days prior to experiments. This concentration blocked cell cycle while limiting cell death.

Spreading assay and TIRF imaging. Before experiments, cells were trypsinized, and maintained under smooth agitation for at least 2 h at 37 °C in medium containing DMEM without Phenol red, supplemented with 10% FBS and 15µL/mL Hepes. Cells were then released in an imaging chamber containing the same medium as during incubation maintained at 37°C. TIRF imaging of spreading was performed every 30s through a PlanApo 100X/1.45 oil objective and a F-View CCD camera (Olympus) using an IX-71 Olympus microscope coupled to a monochromatic (GFP, 450–480 nm) TIRF arm. For the parallel plate assay, a glass micro-plate was brought above the cell just before onset of spreading thanks to piezo-electric translation stages interfaced on a 3-axis micro-manipulator (PhysikeInstrumente). The glass micro-plate was pulled from rectangular plates using a micropipette puller (PB-7; Narishige) and adjusted with a microforge (MF-900; Narishige); they were then attached to a bent glass capillary and connected to a micro-manipulation apparatus prior to experiment. The bottom of the imaging chamber and the glass micro-plate were incubated in DMEM containing 5 µg/mL fibronectin (F1141; Sigma-Aldrich) prior to experiment to promote specific cell adhesion. In order to inhibit cell contractility, cells were agitated in presence of Y-27632 at 8µM (Sigma- Aldrich) 30 min before the beginning of the experiments. To ensure that symmetric spreading occurred on both plates (as observed in the profile parallel plates setup), attachment to the upper plate was tested at the end of each experiment by pulling on it with the micro-manipulator and further checked through bright field imaging of the experiment (see Methods in (22)).

Spreading assay and profile imaging. For profile imaging of spreading in bright-field, the cells were prepared as described above. For the parallel plates assay, two glass micro-plates fabricated and coated as described above were positioned at the bottom of the chamber parallel to each other and brought in contact with the cell before to be lifted. For spreading on a single plate, the same micro-plate was aligned perpendicularly to the bottom of the imaging chamber and positioned in contact with the cell. To avoid cell spreading at the bottom of the imaging chamber, a thin layer of PDMS (about 10 µm) was spin-coated on the glass coverslip and coated with Pluronic (1% in water; F127TM; Sigma-Aldrich) for 1h after plasma cleaning.

Spreading was imaged every 10s through bright-field imaging using a CMOS camera (ORCA-Flash 4.0, Hamamatsu) and a 60X water objective (UPLSAPO, Olympus) mounted on an Olympus IX81 inverted microscope.

Measurement and characterization of cell contact area. Methods for segmentation and transitions in cell-substrate contact area and paxillin organization were thoroughly described in (22). Briefly, for the determination of the cell–substrate contact area from TIRF images of paxillin-YFP, an ImageJ custom-built macro was used. Noise was removed using the functions : *Despeckle*, *Smooth*, *Subtract Background* before binarization of the image through a threshold in intensity manually defined. To include some potentially isolated parts, we then used the closure algorithm *Close-*. The contact area $A(t_R^*)$ corresponding to the transition in spreading regimes was defined as the largest contact radius $R(t) = \sqrt{\frac{A(t)}{\pi}}$ before $R(t)$ departed from a linear

trend.

Segmentation of FA clusters. The regions covered with FA clusters were defined according to a threshold in intensity from TIRF images of paxillin-YFP. For that, the entropy-based algorithm *RenyiEntropy* (48) based on the entropic analysis of the intensity histogram of the image and implemented in ImageJ was used. During the early phase of spreading ($t < t_{\text{adh}}^*$), the algorithm detected a region corresponding to the entire contact area, indicating that no region of the contact was specifically intense. We noted $A(t_{\text{adh}}^*)$, the contact area retrieved from the last frame devoid of adhesion clusters. Then, we noted S_{pax} the area of the peripheral ring of intense paxillin-YFP clusters measured after 20 minutes of spreading.

Individual FA clusters were segmented manually. A minimum of 8 clusters per cell were selected based on their aspect ratio (which was chosen superior to 1.8) and on their location (within FA ring). The average FA area was then calculated for each cell tested.

Determination of the width of the FA ring. To measure mean paxillin intensity with respect to the distance to cell edge, we use the *Erosion* algorithm of *ImageJ*. Because the erosion in ImageJ is performed with a square 3×3 structuring element, the distance from the leading edge of the n-th concentric region is best approximated as $d \simeq n d_{\text{pix}} \sqrt{2}$ where d_{pix} is the pixel size. Next, we plotted the mean fluorescence intensity $I_{\text{raw}}(d,t)$ of these concentric regions as a kymograph. In order to detect the distance from which the signal significantly decreases, we first normalized the signal I_{raw} by an affine mapping, $I_{\text{norm}} = (I_{\text{raw}} - I_{\text{raw}}^1)(I_{\text{raw}}^9 - I_{\text{raw}}^1)$ where the I_{raw}^i are the i-th decile value of I_{raw}. Next we detected the distance from edge $\tilde{W}_r(t)$ where I_{norm} crossed the value 0.5 for the first time while decreasing,

$$\tilde{W}_r(t) = \min\{d, I_{\text{norm}}(d,t) = 0.5 \text{ and } \partial_d I_{\text{norm}} < 0\}.$$

Since occasional large variations are possible over a single frame, we applied a median filter with a window size of 3 in order to define w_r,

$$W_r(t) = \text{median}\left\{(\tilde{W}_r(t - \Delta t), \tilde{W}_r(t), \tilde{W}_r(t + \Delta t)\right\}.$$

Segmentation of cell profile and measurement of contact angle. To measure the shape changes of cells profile during spreading, an ad-hoc python algorithm was developed. First, to make the glass plate appear horizontal on the image, a rotation of the image is applied (using a linear Hough transform to detect the glass edge original angle). Optical aberration generated by the glass plate in the cell region is then removed by subtracting to each vertical line of the image the typical profile of the shadow computed from a region of the image free of cell. Finally, the profile of the cell is segmented using the active contour method (49) implemented in the *scikit-image* library (50). After a manual initialization of the cell contour on the first frame, the contour is re-adjusted in each successive image to the new cell shape using the active contour method. These contours are analyzed to determine the geometrical descriptors of the cell shape on each

frame (see Fig. 3C). The dorsal arc radius is extracted by fitting an arc of circle to the upper part (representing 2/3 of cell height) of the cell body. The cell body contact diameter is calculated from the two points of the contour on each side of the cell reaching a distance to the plate $\leq 0{,}75\mu$m. Finally, the macroscopic cell contact angle is determined from the tangent to the contour at the point of inversion of cell contour curvature. For that, the local curvature of the cell contour κ was computed along the contour expressed parametrically as $(\text{x(t), y(t)}) : \kappa = \frac{|x''y' - x'y''|}{(y'^2 + x'^2)^{\frac{3}{2}}}$. The tangent of the cell contour around this position is subsequently obtained from a linear fit along a 1 μm contour length.

Confocal imaging. For confocal imaging of fixed cells at various stages of spreading, cells were fixed with paraformaldehyde (15 min; 3% in PBS), permeabilized in Triton X-100 (15 min; 0.2% in PBS), and put in presence of BSA (30 min; 1% in PBS). For actin staining, cells were incubated with fluorescent phalloidin from Fluoprobes (30 min; 0.1% in PBS). Cells were imaged using a confocal spinning disk from Andor Technology coupled to an Olympus IX-81 microscope with a 60X oil objective.

The lamella width and cell body radius were measured based on the same criterion as for the determination of the cell body radius in profile bright-field imaging of spreading: the extremities of the cell body diameter were defined from the two points of the contour on each side of the cell reaching a distance to the substrate $\leq 0{,}75\mu$m. The lamella width W_l was then calculated from the total cell contact area A measured independently and through the equation $A = \pi(W_l + R_b)^2$, with R_b the cell body radius.

Bibliography

1. Alejandro E Mayorca-Guiliani, Chris D Madsen, Thomas R Cox, Edward R Horton, Freja A Venning, and Janine T Erler. Isdot: in situ decellularization of tissues for high-resolution imaging and proteomic analysis of native extracellular matrix. *Nature medicine*, 23(7):890–898, 2017.

2. Esther Wershof, Danielle Park, Robert P Jenkins, David J Barry, Erik Sahai, and Paul A Bates. Matrix feedback enables diverse higher-order patterning of the extracellular matrix. *PLoS computational biology*, 15(10):e1007251, 2019.

3. Paolo P Provenzano, Kevin W Eliceiri, Jay M Campbell, David R Inman, John G White, and Patricia J Keely. Collagen reorganization at the tumor-stromal interface facilitates local invasion. *BMC medicine*, 4(1):1–15, 2006.

4. Brendon M Baker and Christopher S Chen. Deconstructing the third dimension–how 3d culture microenvironments alter cellular cues. *Journal of cell science*, 125(13):3015–3024, 2012.

5. Jing Xie, Min Bao, Stéphanie MC Bruekers, and Wilhelm TS Huck. Collagen gels with different fibrillar microarchitectures elicit different cellular responses. *ACS applied materials & interfaces*, 9(23):19630–19637, 2017.

6. John L Tan, Joe Tien, Dana M Pirone, Darren S Gray, Kiran Bhadriraju, and Christopher S Chen. Cells lying on a bed of microneedles: an approach to isolate mechanical force. *Proceedings of the National Academy of Sciences*, 100(4):1484–1489, 2003.

7. Rowena McBeath, Dana M Pirone, Celeste M Nelson, Kiran Bhadriraju, and Christopher S Chen. Cell shape, cytoskeletal tension, and rhoa regulate stem cell lineage commitment. *Developmental cell*, 6(4):483–495, 2004.

8. Christopher S Chen, Milan Mrksich, Sui Huang, George M Whitesides, and Donald E Ingber. Geometric control of cell life and death. *Science*, 276(5317):1425–1428, 1997.

9. Amandine Pitaval, Qingzong Tseng, Michel Bornens, and Manuel Théry. Cell shape and contractility regulate ciliogenesis in cell cycle–arrested cells. *Journal of Cell Biology*, 191 (2):303–312, 2010.

10. Xian Zhang, Guoying Jiang, Yunfei Cai, Susan J Monkley, David R Critchley, and Michael P Sheetz. Talin depletion reveals independence of initial cell spreading from integrin activation and traction. *Nature cell biology*, 10(9):1062–1068, 2008.

11. Margaret L Gardel, Benedikt Sabass, Lin Ji, Gaudenz Danuser, Ulrich S Schwarz, and Clare M Waterman. Traction stress in focal adhesions correlates biphasically with actin retrograde flow speed. *Journal of Cell Biology*, 183(6):999–1005, 2008.

12. Ana M Pasapera, Ian C Schneider, Erin Rericha, David D Schlaepfer, and Clare M Waterman. Myosin ii activity regulates vinculin recruitment to focal adhesions through fak-mediated paxillin phosphorylation. *Journal of Cell Biology*, 188(6):877–890, 2010.

13. Benjamin Geiger, Joachim P Spatz, and Alexander D Bershadsky. Environmental sensing through focal adhesions. *Nature reviews Molecular cell biology*, 10(1):21–33, 2009.

14. Antonina Y Alexandrova, Katya Arnold, Sébastien Schaub, Jury M Vasiliev, Jean-Jacques Meister, Alexander D Bershadsky, and Alexander B Verkhovsky. Comparative dynamics of retrograde actin flow and focal adhesions: formation of nascent adhesions triggers transition from fast to slow flow. *PloS one*, 3(9):e3234, 2008.

15. Marion Ghibaudo, Alexandre Saez, Léa Trichet, Alain Xayaphoummine, Julien Browaeys, Pascal Silberzan, Axel Buguin, and Benoît Ladoux. Traction forces and rigidity sensing regulate cell functions. *Soft Matter*, 4(9):1836–1843, 2008.

16. Kalpana Mandal, Irène Wang, Elisa Vitiello, Laura Andreina Chacòn Orellana, and Martial Balland. Cell dipole behaviour revealed by ecm sub-cellular geometry. *Nature communications*, 5(1):1–10, 2014.

17. Guillaume Salbreux, Guillaume Charras, and Ewa Paluch. Actin cortex mechanics and cellular morphogenesis. *Trends in cell biology*, 22(10):536–545, 2012.

18. M Lisa Manning, Ramsey A Foty, Malcolm S Steinberg, and Eva-Maria Schoetz. Coaction of intercellular adhesion and cortical tension specifies tissue surface tension. *Proceedings of the National Academy of Sciences*, 107(28):12517–12522, 2010.

19. Jean-Léon Maître, Ritsuya Niwayama, Hervé Turlier, François Nédélec, and Takashi Hiiragi. Pulsatile cell-autonomous contractility drives compaction in the mouse embryo. *Nature cell biology*, 17(7):849–855, 2015.

20. Kazunori Yamamoto, Sacha Ichbiah, Matthieu Perez, Joana Borrego-Pinto, Fabrice Delbary, Nate Goehring, Hervé Turlier, and Guillaume Charras. Spatiotemporal mapping of the contractile and adhesive forces sculpting early c. elegans embryos. *bioRxiv*, pages 2023–03, 2023.

21. Dylan T Burnette, Lin Shao, Carolyn Ott, Ana M Pasapera, Robert S Fischer, Michelle A Baird, Christelle Der Loughian, Helene Delanoe-Ayari, Matthew J Paszek, Michael W Davidson, et al. A contractile and counterbalancing adhesion system controls the 3d shape of crawling cells. *Journal of Cell Biology*, 205(1):83–96, 2014.

22. Jonathan Fouchard, Célian Bimbard, Nathalie Bufi, Pauline Durand-Smet, Amsha Proag, Alain Richert, Olivier Cardoso, and Atef Asnacios. Three-dimensional cell body shape dictates the onset of traction force generation and growth of focal adhesions. *Proceedings of the National Academy of Sciences*, 111(36):13075–13080, 2014.

23. Franck Raynaud, Mark E Ambühl, Chiara Gabella, Alicia Bornert, Ivo F Sbalzarini, Jean-Jacques Meister, and Alexander B Verkhovsky. Minimal model for spontaneous cell polarization and edge activity in oscillating, rotating and migrating cells. *Nature Physics*, 12(4): 367–373, 2016.

24. Zeno Messi, Alicia Bornert, Franck Raynaud, and Alexander B Verkhovsky. Traction forces control cell-edge dynamics and mediate distance sensitivity during cell polarization. *Current Biology*, 30(9):1762–1769, 2020.

25. Hans-Günther Döbereiner, Benjamin Dubin-Thaler, Grégory Giannone, Harry S Xenias, and Michael P Sheetz. Dynamic phase transitions in cell spreading. *Physical review letters*, 93 (10):108105, 2004.

26. Damien Cuvelier, Manuel Théry, Yeh-Shiu Chu, Sylvie Dufour, Jean-Paul Thiéry, Michel Bornens, Pierre Nassoy, and L Mahadevan. The universal dynamics of cell spreading. *Current biology*, 17(8):694–699, 2007.

27. MA Fardin, OM Rossier, P Rangamani, PD Avigan, NC Gauthier, W Vonnegut, A Mathur, J Hone, R Iyengar, and MP Sheetz. Cell spreading as a hydrodynamic process. *Soft matter*, 6(19):4788–4799, 2010.

28. Demosthene Mitrossilis, Jonathan Fouchard, Axel Guiroy, Nicolas Desprat, Nicolas Rodriguez, Ben Fabry, and Atef Asnacios. Single-cell response to stiffness exhibits muscle-like behavior. *Proceedings of the National Academy of Sciences*, 106(43):18243–18248, 2009.

29. Léa Trichet, Jimmy Le Digabel, Rhoda J Hawkins, Sri Ram Krishna Vedula, Mukund Gupta, Claire Ribrault, Pascal Hersen, Raphaël Voituriez, and Benoît Ladoux. Evidence of a large-scale mechanosensing mechanism for cellular adaptation to substrate stiffness. *Proceedings of the National Academy of Sciences*, 109(18):6933–6938, 2012.

30. Démosthène Mitrossilis, Jonathan Fouchard, David Pereira, François Postic, Alain Richert, Michel Saint-Jean, and Atef Asnacios. Real-time single-cell response to stiffness. *Proceedings of the national academy of sciences*, 107(38):16518–16523, 2010.

31. Ewa Zlotek-Zlotkiewicz, Sylvain Monnier, Giovanni Cappello, Mael Le Berre, and Matthieu Piel. Optical volume and mass measurements show that mammalian cells swell during mitosis. *Journal of Cell Biology*, 211(4):765–774, 2015.

32. Clotilde Cadart, Larisa Venkova, Pierre Recho, Marco Cosentino Lagomarsino, and Matthieu Piel. The physics of cell-size regulation across timescales. *Nature Physics*, 15 (10):993–1004, 2019.

33. Pedro Echave, Ian J Conlon, and Alison C Lloyd. Cell size regulation in mammalian cells. *Cell cycle*, 6(2):218–224, 2007.

34. Yukiaki Kuroda and Junichi Furuyama. Physiological and biochemical studies of effects of mitomycin c on strain hela cells in cell culture. *Cancer research*, 23(5):682–687, 1963.

35. Tom Shemesh, Alexander D Bershadsky, and Michael M Kozlov. Physical model for self-organization of actin cytoskeleton and adhesion complexes at the cell front. *Biophysical journal*, 102(8):1746–1756, 2012.

36. Neil Ibata and Eugene M Terentjev. Development of nascent focal adhesions in spreading cells. *Biophysical journal*, 119(10):2063–2073, 2020.

37. Yunfei Cai, Olivier Rossier, Nils C Gauthier, Nicolas Biais, Marc-Antoine Fardin, Xian Zhang, Lawrence W Miller, Benoit Ladoux, Virginia W Cornish, and Michael P Sheetz. Cytoskeletal coherence requires myosin-iia contractility. *Journal of cell science*, 123(3):413–423, 2010.

38. Jean-Léon Maître, Hélène Berthoumieux, Simon Frederik Gabriel Krens, Guillaume Salbreux, Frank Jülicher, Ewa Paluch, and Carl-Philipp Heisenberg. Adhesion functions in cell sorting by mechanically coupling the cortices of adhering cells. *Science*, 338:253–256, 2012. doi: 10.1126/science.1225399.

39. Grégory Giannone, Benjamin J Dubin-Thaler, Hans-Günther Döbereiner, Nelly Kieffer, Anne R Bresnick, and Michael P Sheetz. Periodic lamellipodial contractions correlate with rearward actin waves. *Cell*, 116(3):431–443, 2004.

40. Samuel Bell, Anna-Lena Redmann, and Eugene M Terentjev. Universal kinetics of the onset of cell spreading on substrates of different stiffness. *Biophysical journal*, 116(3):551–559, 2019.

41. Nils C Gauthier, Marc Antoine Fardin, Pere Roca-Cusachs, and Michael P Sheetz. Temporary increase in plasma membrane tension coordinates the activation of exocytosis and contraction during cell spreading. *Proceedings of the National Academy of Sciences*, 108 (35):14467–14472, 2011.

42. Salma Jalal, Shidong Shi, Vidhyalakshmi Acharya, Ruby Yun-Ju Huang, Virgile Viasnoff, Alexander D Bershadsky, and Yee Han Tee. Actin cytoskeleton self-organization in single epithelial cells and fibroblasts under isotropic confinement. *Journal of cell science*, 132(5): jcs220780, 2019.

43. Alexander W Shingleton, W Anthony Frankino, Thomas Flatt, H Frederik Nijhout, and Douglas J Emlen. Size and shape: the developmental regulation of static allometry in insects. *BioEssays*, 29(6):536–548, 2007.

44. Alice E Maher, Gustavo Burin, Philip G Cox, Thomas W Maddox, Susannah CR Maidment, Natalie Cooper, Emma R Schachner, and Karl T Bates. Body size, shape and ecology in tetrapods. *Nature Communications*, 13(1):4340, 2022.

45. Yee-Hung M Chan and Wallace F Marshall. Scaling properties of cell and organelle size. *Organogenesis*, 6(2):88–96, 2010.

46. David Labonte, Christofer J Clemente, Alex Dittrich, Chi-Yun Kuo, Alfred J Crosby, Duncan J Irschick, and Walter Federle. Extreme positive allometry of animal adhesive pads and the size limits of adhesion-based climbing. *Proceedings of the National Academy of Sciences*, 113(5):1297–1302, 2016.

47. Eliana Marinari, Aida Mehonic, Scott Curran, Jonathan Gale, Thomas Duke, and Buzz Baum. Live-cell delamination counterbalances epithelial growth to limit tissue overcrowding. *Nature*, 484(7395):542–545, 2012.

48. Jagat Narain Kapur, Prasanna K Sahoo, and Andrew KC Wong. A new method for gray-level picture thresholding using the entropy of the histogram. *Computer vision, graphics, and image processing*, 29(3):273–285, 1985.

49. Michael Kass, Andrew Witkin, and Demetri Terzopoulos. Snakes: Active contour models. *International journal of computer vision*, 1(4):321–331, 1988.

50. Stefan Van der Walt, Johannes L Schönberger, Juan Nunez-Iglesias, François Boulogne, Joshua D Warner, Neil Yager, Emmanuelle Gouillart, and Tony Yu. scikit-image: image processing in python. *PeerJ*, 2:e453, 2014.
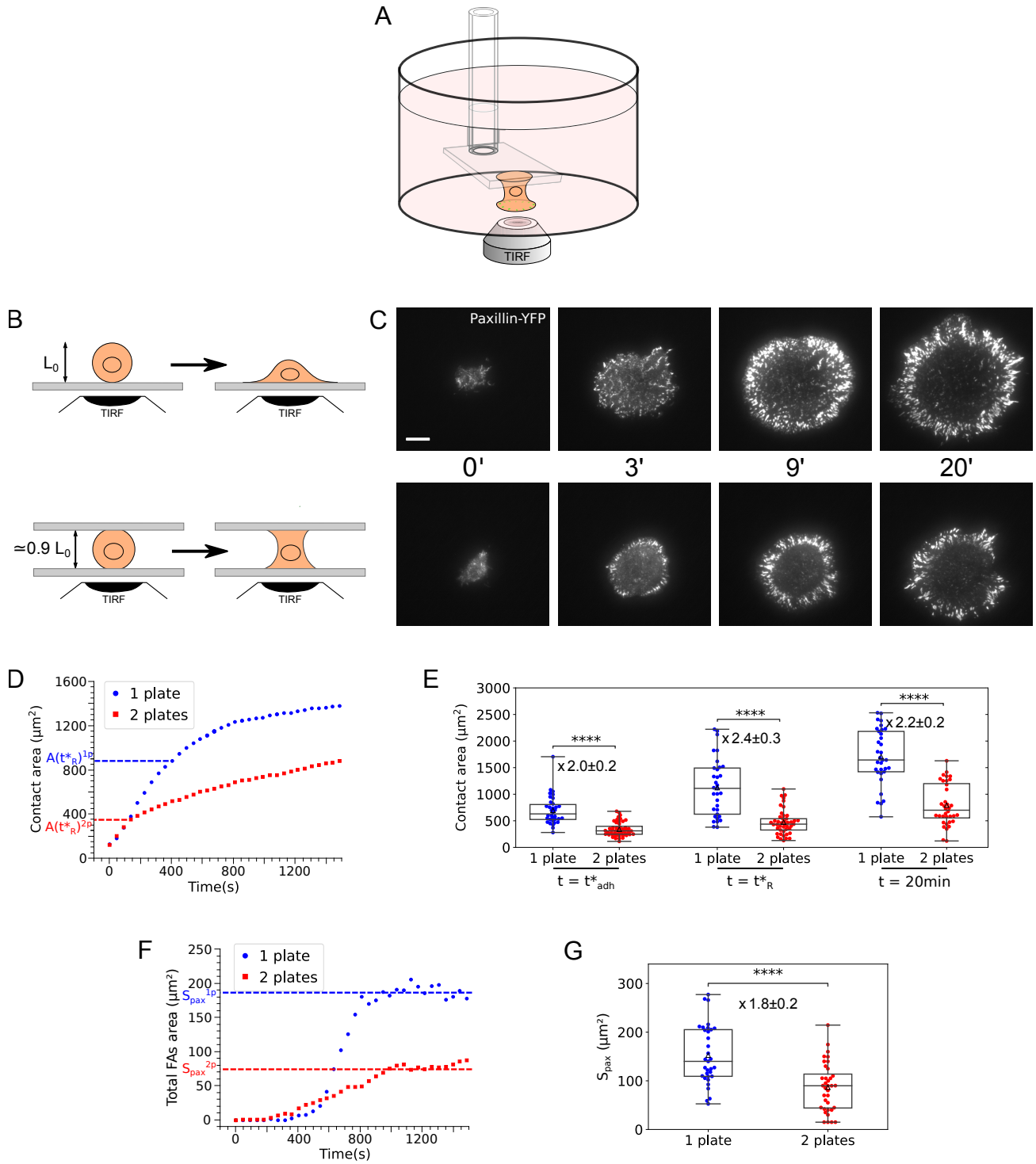
Fig. 1. A – Diagram depicting the parallel plate experiment for the analysis of spreading in condition of third-dimension confinement. A microplate parallel to the bottom of the chamber is brought in contact with the cell just after sedimentation and before spreading onset. The contact with the bottom of the chamber is imaged by TIRF microscopy. B – Diagram representing cell spreading configurations for TIRF imaging. Top: A cell in suspension is let free to spread on a uniform bi-dimensional glass substrate. Bottom: A cell is let free to spread between two parallel plates, separated by about 90% of original cell length L_0. C – TIRF imaging of cell-substrate contact of the early spreading of Ref-52 fibroblasts expressing Paxillin-YFP in the two confinement configurations, as described in B. Scale bar : 5μm. D – Typical evolution of cell-substrate contact area for the single plate (blue) and parallel plates geometry (red). E – Boxplots of characteristic cell-substrate contact areas of cell spreading in the two substrate geometrical configurations. Left: Contact area $A(t^*_{adh})$ indicating onset of focal adhesions-like paxillin clusters formation. Middle: Contact area $A(t^*_R)$ characterizing slow-down of spreading. Right: Contact area $A(t = 20min)$ after 20 minutes of spreading. F – Typical evolution of the integrated area of FA ring for the single plate (blue) and parallel plates geometry (red). G – Boxplot representing the cumulated area of FAs S_{pax} after 20 minutes of spreading.
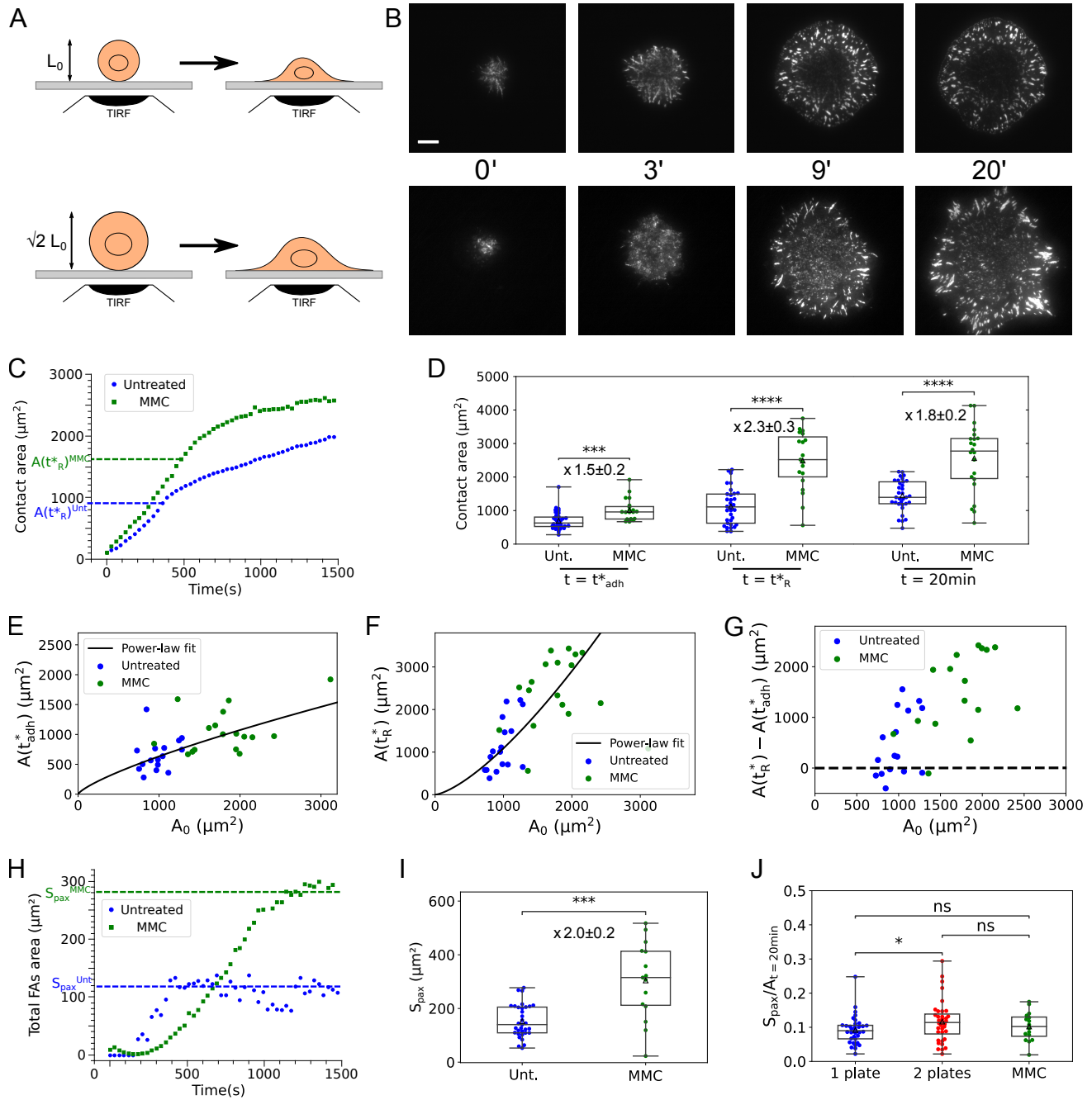
Fig. 2. A – Spreading of cells with different size. Top: Untreated cells, normal cell size. Bottom: Cells treated with mitomycin C, large cell size. (Cell volume is increased 2.8 times on average.) **B** – TIRF imaging of cell-substrate contact of the early spreading of Ref-52 fibroblasts expressing paxillin-YFP in untreated cells (top) and cells treated with mitomycin C (bottom). Scale bar : 5μm. **C** – Typical evolution of cell-substrate contact area in untreated (blue) and mitomycin C-treated (green) cells. **D** – Boxplots of characteristic cell-substrate contact areas of cell spreading in untreated and mitomycin C-treated cells. Left: Contact area $A(t^*_{adh})$ indicating onset of FA-like paxillin clusters formation. Middle: Contact area $A(t^*_R)$ characterizing slow-down of spreading. Right: Contact area $A(t = 20min)$ after 20 minutes of spreading. **E** – Contact area $A(t^*_{adh})$ as a function of cell surface in suspension A_0 in untreated (blue) and Mitomycin-C treated cells (green). Dotted line: power-law fit. **F** – Contact area $A(t^*_R)$ as a function of cell surface in suspension A_0 in untreated (blue) and Mitomycin C treated cells (green). Dotted line: power-law fit. **G** – Difference between spreading slow-down and onset of focal adhesions-like clusters formation contact areas as a function of cell surface in suspension A_0. **H** – Typical evolution of the cumulated area of FAs for untreated (blue) and mitomycin C-treated cells (green). **I** – Boxplot representing the cumulated area of FAs after 20 minutes of spreading for untreated (blue) and mitomycin C-treated cells (green). **J** – Boxplot representing the ratio of the cumulated area of FAs over cell-substrate contact area for untreated cells spreading on a single plate (1 plate), MMC-treated cells spreading on a single plate (1 plate - MMC) and for untreated cells spreading between two parallel plates (2 plates) after 20 minutes of spreading.
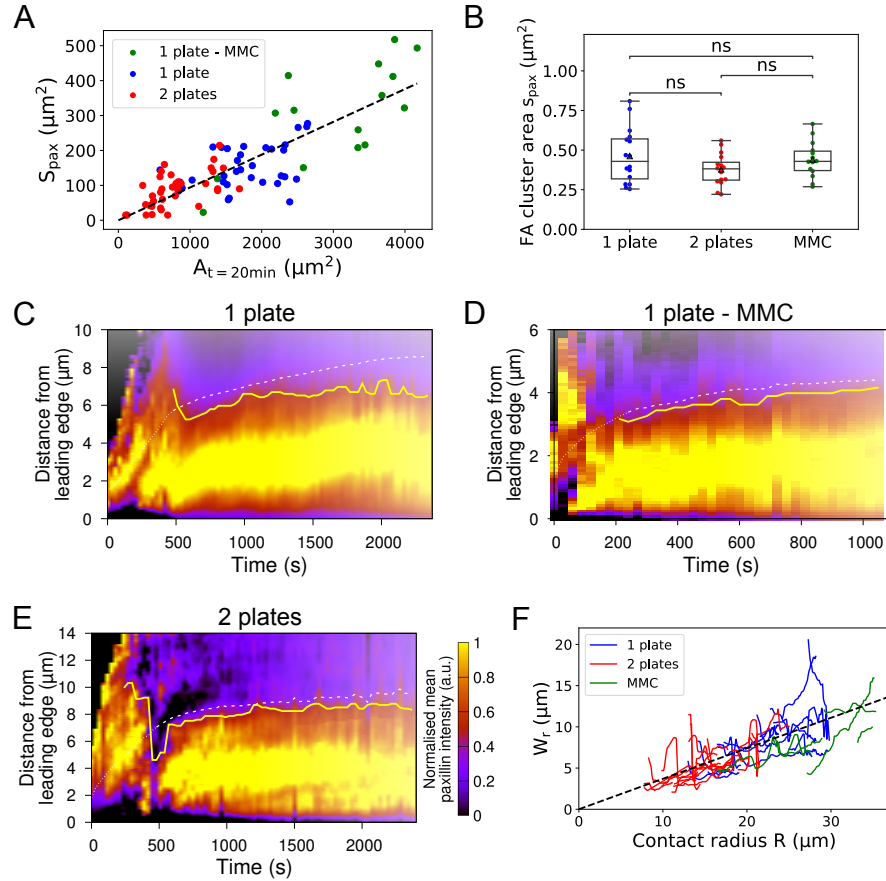
Fig. 3. A – Cumulated area of FAs S_{pax} as a function of cell contact area A after 20 min of spreading for untreated cells spreading on a single plate (1 plate), mitomycin C-treated cells spreading on a single plate (1 plate - MMC) and for untreated cells spreading between two parallel plates (2 plates). B – Individual paxillin clusters area s_{pax}. Each point represent the average for an individual cell over N=8 clusters. C - Kymograph of normalized paxillin intensity as a function of the distance to the cell edge and along time for a cell spreading on a single plate. Solid yellow line: paxillin ring width W_r. Dashed white line: estimation of W_l from allometry relation $W_l = \beta/(1+\beta)R$ (see Fig. 7B). D- Same as Fig. C for a cell treated with mitomycin C and spreading on a single plate. E - Same as Fig. C for a cell spreading between parallel plates. F - Width of the focal adhesions ring versus contact radius along the second phase of spreading P2 for untreated cells in single plate geometry (blue), parallel plates geometry (red) and MMC treated cells in single plate geometry (green). Each line represent one sample.
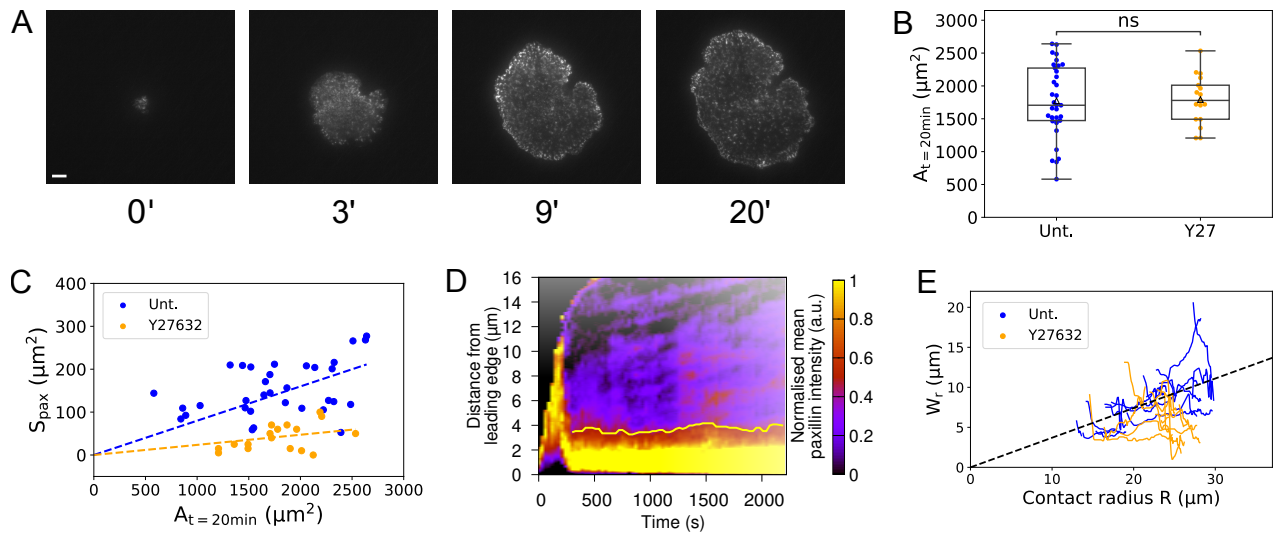

Fig. 4. A – TIRF imaging of cell-substrate contact of the early spreading of Ref-52 fibroblasts expressing paxillin-YFP treated with 8μM of the Rho kinase inhibitor Y27632 cells. Scale bar : 5μm. B - Boxplot of cell contact area after 20 minutes of spreading in untreated cells and Y277632 treated cells (Y27). C - Cumulated area of FAs S_{pax} as a function of cell contact area after 20 min of spreading for untreated cells spreading on a single plate (blue) and Y27632-treated cells (orange). Dotted lines represent the linear regression crossing the origin for each populations with coefficient 8.0×10^{-2} and 2.4×10^{-2} respectively. D - Kymograph of normalized paxillin intensity as a function of the distance to the cell edge and along time for a cell treated with Y27632, spreading on a single plate. Solid yellow line: paxillin ring width W_r. E - Width of the focal adhesions ring versus contact radius along the second phase of spreading P2 for untreated cells in single plate geometry (blue) and Y27632 treated cells in single plate geometry (orange). Each line represent one sample.
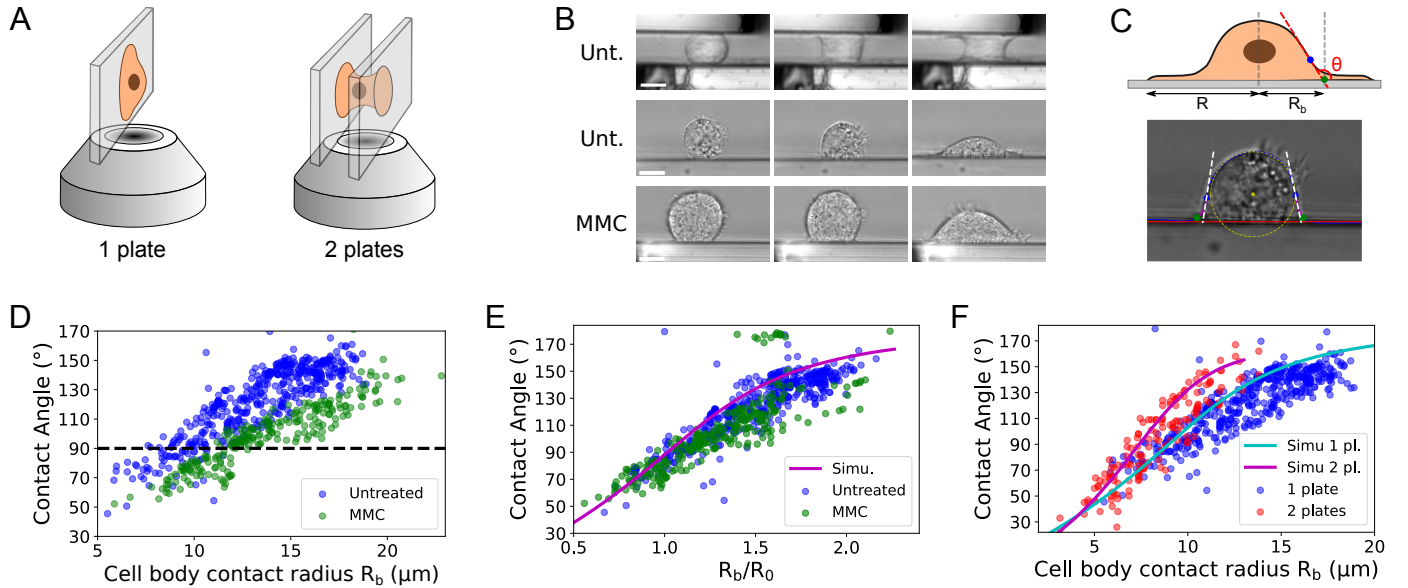
Fig. 5. A – Diagram representing imaging configuration of cell spreading imaged in profile. Left: Spreading on a single glass plate, aligned perpendicularly to the objective focal plane. Right: Profile imaging in the parallel plates assay. B – Profile imaging of a cell spreading between parallel plates (top), on a single plate (middle) and a mitomycin C-treated cell spreading on a single plate (bottom). Scale bar: 10µm. C – Diagram and picture showing the definitions used for cell contact angle and cell body contact radius. D – Cell contact angle θ as a function of cortex contact radius R_b for untreated (blue, N=10) and mitomycin C-treated cells (green, N=4) . E – Cell contact angle as a function of cell body contact radius R_b normalized by cell radius in suspension R_0. The solid line represents the behavior of a spherical cap of constant volume (see also Fig. 6). F – Cell contact angle θ as a function of cell body contact radius R_b for cell spreading on a single plate (blue) or in between parallel plates (red, N=6). The solid lines represents the behaviors of geometrical models as described in the main text (see also Fig. 6).
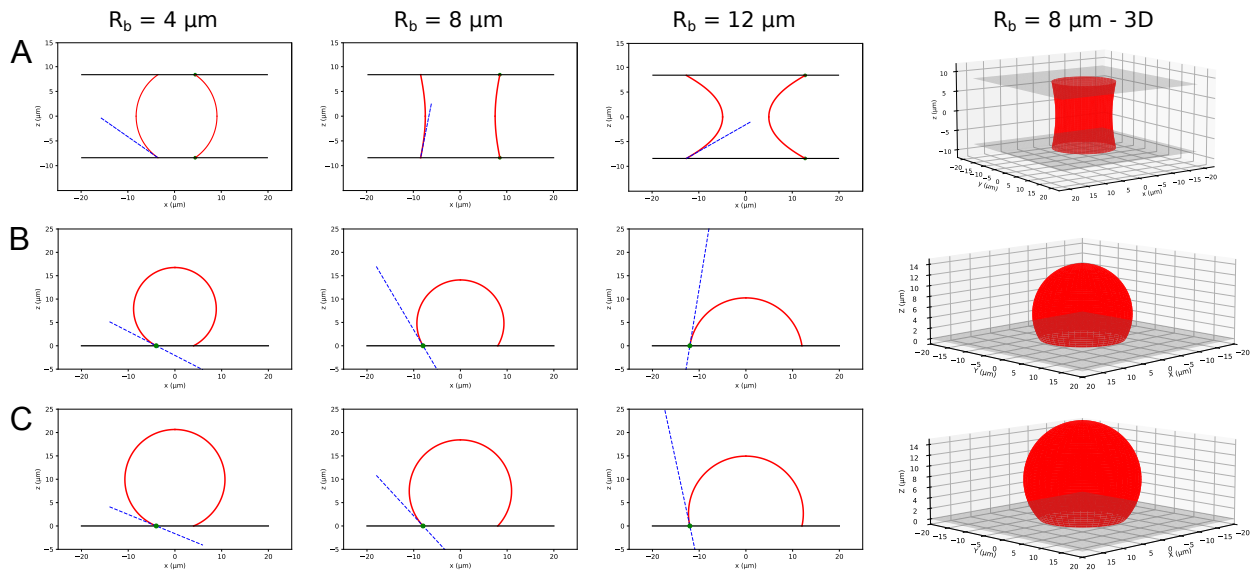

Fig. 6. Geometrical modeling of three-dimensional cell shape changes during spreading using constant mean curvature surfaces. The first three columns show a cross-section of the predicted cell shape, for three typical contact radii ($R_b = 4µm, 8µm$ and $12µm$). The column on the right shows a 3D representation of cell shape prediction for a contact radius $R_b = 8µm$. A – Prediction of cell shape changes during spreading between parallel plates (black lines). Free edges (red lines) are modeled by a nodoid or unduloid in contact with the plates. Blue dotted lines indicate the tangent to the free edge at the contact point with the plate, defining the contact angle. B – Same as A for a spherical cap (red line) model mimicking cell spreading on a bi-dimensional substrate (black line). C – Same as B for a spherical cap of larger initial volume, mimicking spreading under mitomycin C treatment.
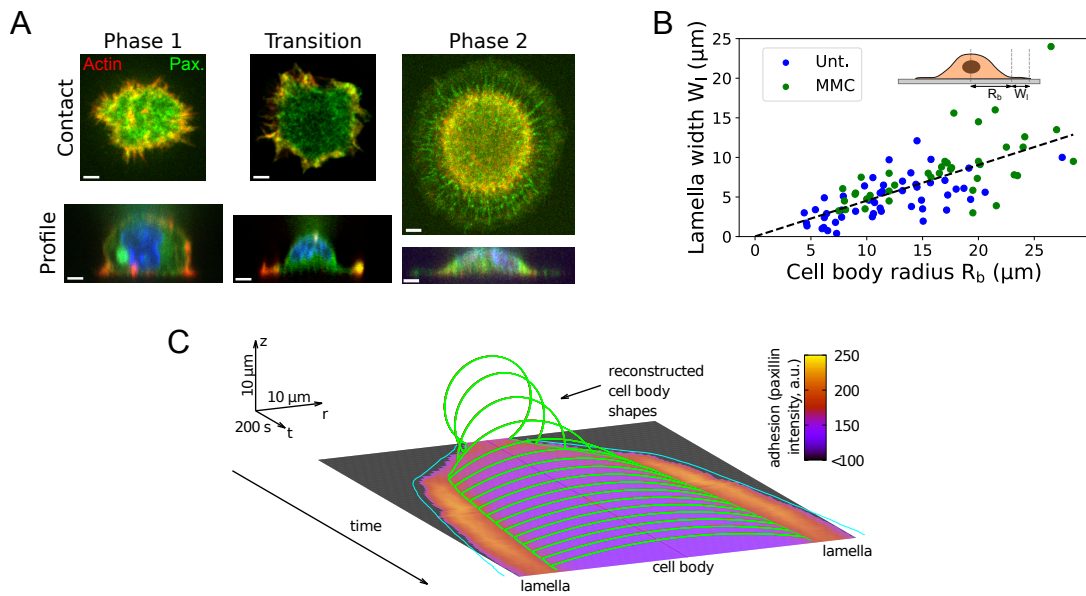
Fig. 7. A – Cell shape (profile and cell-substrate contact) imaged through confocal imaging of spreading cells fixed at different stages of spreading. Scale bars: 5µm. B – Lamella width W_l as a function of cell body contact radius R_b for untreated (blue) and mitomycin C-treated cells (green). C - Reconstructed cell body shapes and lamella growth along spreading (for the sample analyzed in Fig. 3C). The averaged spatial distribution of paxillin intensity along time is shown at the cell-substrate interface.